CHEMISTRY OF MATERIALS
Article

Chem. Mater. **2010,** *22,* 4679–4689 4679
DOI:10.1021/cm100886y

Properties and Functions of Hierarchical Ferrierite Zeolites Obtained by Sequential Post-Synthesis Treatments

Danny Verboekend,[†] Rosario Caicedo-Realpe,[‡] Adriana Bonilla,[‡] Marta Santiago,[†] and Javier Pérez-Ramírez*[,†,‡,§]

[†]*Institute for Chemical and Bioengineering, Department of Chemistry and Applied Biosciences, ETH Zurich, HCI E 125, Wolfgang-Pauli-Strasse 10, CH-8093, Zurich, Switzerland,* [‡]*Institute of Chemical Research of Catalonia (ICIQ), Avinguda dels Països Catalans 16, 43007, Tarragona, Spain, and* [§]*Catalan Institution for Research and Advanced Studies (ICREA), Passeig de Lluís Companys 16, 08020, Barcelona, Spain*

Received March 29, 2010. Revised Manuscript Received May 21, 2010

A post-synthesis route involving a sequence of up to three treatments in aqueous $NaAlO_2$, HCl, and NaOH solutions, was designed to prepare a variety of complex hierarchical ferrierite zeolites, that is, microporous materials with auxiliary mesoporosity. The precise effect of each step on the composition, structure, morphology, porosity, and acidity of the samples was assessed by means of a multitechnique approach, including inductively coupled plasma-optical emissions spectrometry (ICP-OES), N_2 sorption at 77 K, Ar sorption at 87 K, transmission electron microscopy (TEM), energy dispersive X-ray (EDX) analysis, X-ray diffraction (XRD), liquid and solid-state nuclear magnetic resonance (NMR), Fourier transform infrared spectroscopy (FTIR), and temperature-programmed desorption of ammonia (NH_3-TPD). $NaAlO_2$ desilicates a portion of the zeolite crystal by alkaline attack, although most of the extracted silicon is retained in the solid forming nanocrystals because of $Al(OH)_3$ precipitation on the zeolite surface. A subsequent HCl washing removes the aluminum-containing deposit from the composite, uncovering a dual network of mesopores associated with the desilicated ferrierite platelets and the Si-rich nanocrystals. The latter species were selectively dissolved by mild NaOH washing. The impact of the relative amount of micro- and mesoporosity in the zeolites on the transport properties was studied by elution of butane isomers, and the pyrolysis of low-density polyethylene was selected as a model reaction to assess differences in catalytic performance. In addition, spray deposition was applied to support palladium nanoparticles onto selected ferrierite samples. The hierarchical zeolite yielded higher metal dispersion and size uniformity of Pd nanoparticles in comparison with the parent zeolite. Our study shows that an appropriate sequence of post-synthesis treatments comprises a powerful approach to tune the properties and functions of hierarchical zeolites.

1. Introduction

In recent years, new or modified zeolites have been synthesized with improved accessibility and molecular transport by widening the pores and/or shortening the diffusion path length.[1−5] Hierarchical zeolites accomplish the latter task by coupling the native micropores with an auxiliary mesopore network of inter- or intracrystalline nature. The resulting zeolites attract increasing attention since they exhibit improved activity, selectivity, and/or stability in a wide range of catalyzed reactions.[6−12]

The selective extraction of silicon in an alkaline medium (typically NaOH) is a widely used post-synthesis treatment to create mesoporosity in zeolites; its effectiveness has been demonstrated for multiple framework structures, including MFI,[13] MTW,[14] MOR,[15] BEA,[16] AST,[17] FER,[18]

*To whom correspondence should be addressed. Fax: +41 44 633 1405. E-mail: jpr@chem.ethz.ch.

(1) Corma, A. *Chem. Rev.* **1997**, *97*, 2373.
(2) Čejka, J.; Mintova, S. *Catal. Rev. -Sci. Eng.* **2007**, *49*, 457.
(3) Egeblad, K.; Christensen, C. H.; Kustova, M.; Christensen, C. H. *Chem. Mater.* **2008**, *20*, 946.
(4) Pérez-Ramírez, J.; Christensen, C. H.; Egeblad, K.; Christensen, C. H.; Groen, J. C. *Chem. Soc. Rev.* **2008**, *37*, 2530.
(5) Schmidt, W. *ChemCatChem* **2009**, *1*, 53.
(6) Cho, K.; Cho, H. S.; de Ménorval, L.-C.; Ryoo, R. *Chem. Mater.* **2009**, *21*, 5664.
(7) Song, Y.; Zhu, X.; Song, Y.; Wang, Q. *Appl. Catal., A* **2006**, *288*, 69.
(8) Zhao, L.; Shen, B.; Gao, J.; Xu, C. *J. Catal.* **2008**, *258*, 228.
(9) Kox, M. H. F.; Stavitski, E.; Groen, J. C.; Pérez-Ramírez, J.; Kapteijn, F.; Weckhuysen, B. M. *Chem.—Eur. J.* **2008**, *14*, 1718.
(10) Bjørgen, M.; Joensen, F.; Spangsberg Holm, M.; Olsbye, U.; Lillerud, K.-P.; Svelle, S. *Appl. Catal., A* **2008**, *345*, 43.
(11) Mei, C.; Wen, P.; Liu, Z.; Liu, H.; Wang, Y.; Yang, W.; Xie, Z.; Hua, W.; Gao, Z. *J. Catal.* **2008**, *258*, 243.
(12) Kim, J.; Choi, M.; Ryoo, R. *J. Catal.* **2010**, *269*, 228.
(13) Groen, J. C.; Jansen, J. C.; Moulijn, J. A.; Pérez-Ramírez, J. *J. Phys. Chem. B* **2004**, *108*, 13062.
(14) Wei, X.; Smirniotis, P. G. *Microporous Mesoporous Mater.* **2006**, *97*, 97.
(15) Groen, J. C.; Sano, T.; Moulijn, J. A.; Pérez-Ramírez, J. *J. Catal.* **2007**, *251*, 21.
(16) Groen, J. C.; Abelló, S.; Villaescusa, L.; Pérez-Ramírez, J. *Microporous Mesoporous Mater.* **2008**, *114*, 93.
(17) Pérez-Ramírez, J.; Abelló, S.; Villaescusa, L. A.; Bonilla, A. *Angew. Chem., Int. Ed.* **2008**, *47*, 7913.
(18) Bonilla, A.; Baudouin, D.; Pérez-Ramírez, J. *J. Catal.* **2009**, *265*, 170.

© 2010 American Chemical Society
Published on Web 07/27/2010

MWW,[19] IFR,[20] and STF.[21] In addition to mesopore formation, desilication also impacts on the composition and acid site speciation,[22−24] that is, key properties that are intimately related to the catalytic performance. Previous work showed that acid site modification can be decoupled from mesoporosity formation by sequential treatments in NaOH (desilication) and steam or acid (dealumination).[25,26] In fact, nowadays, a large number of post-synthesis treatments are available that do not influence porosity but target specifically to alter the acid speciation[12,25,26] as well as surface properties.[27,28] Therefore it is certain that an appropriate combination and order of post-synthesis treatments comprises a powerful strategy to tailor zeolite catalysts. A particularly appealing advantage of mastering such a post-synthesis toolbox is that it can be implemented over commercial zeolites, so that the potential impact on industrially relevant catalytic applications can be evaluated in the short term with readily available and abundant materials.

Recently, we studied an alternative post-synthesis variant to introduce secondary mesoporosity in ZSM-5 zeolite, comprising treatment in $NaAlO_2$ followed by HCl washing.[29] This two-step approach, adapted from the patent literature,[30] led to hierarchical ZSM-5 with similar mesopore surface area compared to standard NaOH treatment. However, the desilication and pore formation mechanism by NaOH and $NaAlO_2$+HCl was suggested as different in view of the distinct Si/Al ratio of the obtained mesoporous zeolites (19 in NaOH vs 26 in $NaAlO_2$+HCl when starting from Si/Al ratio 27). Our previous study applying $NaAlO_2$ and HCl treatments on ZSM-5 focused on mesopore formation, that is, the functionality of the obtained materials was not assessed. Progress in the precision design of hierarchical porous zeolites requires solid correlations between changes in physicochemical properties and changes in the specific function (adsorption, diffusion, catalysis, etc.).[6,20,24,31]

Part of the present work aimed at gaining deeper insights into the use of aqueous sodium aluminate as desilicating medium. Accordingly, the original two-step $NaAlO_2$+HCl route was executed on the ferrierite zeolite

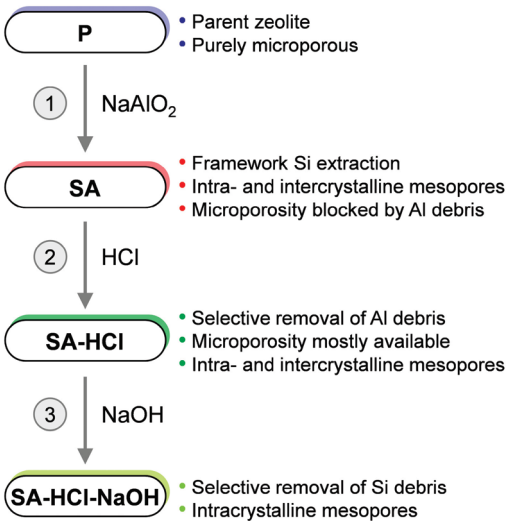

Figure 1. Sequence of post-synthesis treatments over parent ferrierite to prepare hierarchical zeolites. The most important composition and porosity changes of each step are mentioned.

(FER topology) and extended by an additional alkaline washing step in aqueous NaOH to further tune the properties of the material. The FER framework comprises a bidimensional pore network of 10-ring channels (0.42 × 0.54 nm) interconnected with 8-ring channels (0.35 × 0.48 nm).[32] The remarkable selectivity of this zeolite, for example, in the skeletal isomerization of *n*-butene,[33−35] is commonly attributed to the 10-ring pores, as reactant and product molecules cannot enter the 8-ring pores.[36,37] Therefore the controlled introduction of mesoporosity may be highly beneficial to reduce diffusion limitations. Attempts to modify the porous characteristics of ferrierite by dealumination have proven to be sterile.[36−40] The patented route of Garces and Millar[30] led to hierarchical ferrierite with a maximum mesopore surface area (S_{meso}) of 69 $m^2\ g^{-1}$. NaOH leaching of commercial ferrierite with Si/Al = 27 (S_{meso} = 20 $m^2\ g^{-1}$, V_{micro} = 0.14 $cm^3\ g^{-1}$) was screened thoroughly and resulted in a mesopore surface area slightly above 100 $m^2\ g^{-1}$ with 57% of the original micropore volume (V_{micro}) preserved in the hierarchical zeolite.[18]

Herein we have accomplished the synthesis of complex hierarchical porous materials by means of a multistep sequence of three post-synthesis treatments ($NaAlO_2$, HCl, and NaOH) applied to ferrierite (Figure 1). A

(19) Mokrzycki, Ł.; Sulikowski, B.; Olejniczak, Z. *Catal. Lett.* **2009**, *127*, 296.
(20) Verboekend, D.; Groen, J. C.; Pérez-Ramírez, J. *Adv. Funct. Mater.* **2010**, *20*, 1441.
(21) Musilová-Pavlačková, Z.; Zones, S. I.; Čejka, J. *Top. Catal.* **2010**, *53*, 273.
(22) Groen, J. C.; Peffer, L. A. A.; Moulijn, J. A.; Pérez-Ramírez, J. *Chem.—Eur. J.* **2005**, *11*, 4983.
(23) Holm, M. S.; Svelle, S.; Joensen, F.; Beato, P.; Christensen, C. H.; Bordiga, S.; Bjørgen, M. *Appl. Catal., A* **2009**, *356*, 23.
(24) Zhu, X.; Lobban, L. L.; Mallinson, R. G.; Resasco, D. E. *J. Catal.* **2010**, *271*, 88.
(25) Groen, J. C.; Moulijn, J. A.; Pérez-Ramírez, J. *Microporous Mesoporous Mater.* **2005**, *87*, 153.
(26) Fernandez, C.; Stan, I.; Gilson, J.-P.; Thomas, K.; Vicente, A.; Bonilla, A.; Pérez-Ramírez, J. *Chem. Eur. J.* **2010**, *16*, 6224.
(27) Čejka, J.; Žilková, N.; Wichterlová, B.; Eder-Mirth, G.; Lercher, J. A. *Zeolites* **1996**, *17*, 265.
(28) Reitmeier, S. J.; Gobin, O. C.; Jentys, A.; Lercher, J. A. *Angew. Chem., Int. Ed.* **2009**, *48*, 533.
(29) Caicedo-Realpe, R.; Pérez-Ramírez, J. *Microporous Mesoporous Mater.* **2010**, *128*, 91.
(30) Millar, D. M.; Garces, J. M. Patent WO97/15528, 1997.
(31) Pérez-Ramírez, J.; Verboekend, D.; Bonilla, A.; Abelló, S. *Adv. Funct. Mater.* **2009**, *19*, 3972.
(32) Baerlocher, C.; McCusker, L. B.; Olson, D. H. *Atlas of Zeolite Framework Types*, 6th ed.; Elsevier: Amsterdam, 2007.
(33) van Donk, S.; Bitter, J. H.; de Jong, K. P. *Appl. Catal., A* **2001**, *212*, 97.
(34) Vermeiren, W.; Gilson, J.-P. *Top. Catal.* **2009**, *52*, 1131.
(35) Pinar, A. B.; Márquez-Álvarez, C.; Grande-Casas, M.; Pérez-Pariente, J. *J. Catal.* **2009**, *263*, 258.
(36) Onyestyák, Gy.; Valyon, J.; Pál-Borbély, G.; Rees, L. V. C. *Appl. Surf. Sci.* **2002**, *196*, 401.
(37) Cañizares, P.; Carrero, A.; Sánchez, P. *Appl. Catal., A* **2000**, *190*, 93.
(38) Peixoto, D. P. B.; Cabral de Menezes, S. M.; Pais da Silva, M. I. *Mater. Lett.* **2003**, *57*, 3933.
(39) Rachwalik, R.; Olejniczak, Z.; Sulikowski, B. *Catal. Today* **2005**, *101*, 147.
(40) Müller, M.; Harvey, G.; Prins, R. *Microporous Mesoporous Mater.* **2000**, *34*, 135.

Table 1. Notation of the Samples and Treatment Conditions

treatment code	C (M)	T (K)	t (h)
SA1	1	353	3
SA2	1	353	6
SA3	1	363	3
SA4	1	353	0.5
SA5	1	333	3
HCl	3	353	3
NaOH	0.2	333	0.5

thorough characterization provided insights into the composition, structure, morphology, porosity, and acidity of the modified ferrierite zeolites. Important functions were evaluated to quantify the implications of the post-synthesis modifications: (i) the effect on transport was examined by elution experiments with *n*-butane and *i*-butane, (ii) the effect on catalysis was studied by the pyrolysis of low-density polyethylene, and (iii) the effect on metal dispersion was evaluated by spray deposition of palladium nanoparticles onto selected zeolite supports.

2. Experimental Section

Materials and Treatments. Commercial ferrierite zeolite from Zeolyst International (CP 914, lot no. 2200-7, nominal Si/Al = 27, NH_4-form) was converted into the protonic from by calcination in static air at 823 K for 5 h using a heating rate 5 K min^{-1}. The resulting sample, denoted as parent (P), was subjected to individual or consecutive treatments in sodium aluminate (SA*x*), hydrochloric acid (HCl), and sodium hydroxide (NaOH). The treatments (Table 1) were carried out in a round-bottomed flask coupled to a condenser in which the corresponding aqueous solution, stirred at 400 rpm, was heated to the desired temperature. The solid was then added, and the suspension was left to react for the appropriate time. The ratio of sample weight and liquid volume ($m_{sample}/V_{solution}$) was 100 g L^{-1} ($NaAlO_2$ and HCl treatments) or 33 g L^{-1} (NaOH treatment). The treatment was quenched, and the suspension was filtered and washed with distilled water until neutral pH. The resulting solid was dried at 333 K for 12 h after which calcination was performed at the conditions described above for the as-received zeolite. In the case of the SA1-HCl-NaOH sample, final calcination was sometimes preceded by three consecutive treatments in aqueous NH_4NO_3 (0.1 M, 298 K, 12 h) to ensure that the hierarchical zeolite is in the protonic form.

Metal Incorporation by Spray Deposition. Palladium was deposited on selected ferrierite samples using a Mini Spray Dryer B-290 from Büchi equipped with a two-fluid nozzle (diameter 0.7 mm). A suspension of the zeolite in water (20 wt %) was prepared and continuously stirred (400 rpm) at room temperature. Then, an appropriate amount of $Pd(NO_3)_2 \cdot 2H_2O$ (Fluka) was dissolved in the suspension to obtain a Pd loading of 1.3 wt % in the final solid. The slurry was pumped (5 cm^3 min^{-1}) to the nozzle together with the spray air flow (0.4 m^3 h^{-1}). The inlet temperature was set at 493 K, and the aspirator rate at 80%. The hot drying gas (ca. 30 m^3 h^{-1}) flowed concurrently in the spray nozzle direction. The outlet temperature, which is a function of the aspirator rate, inlet temperature, and liquid feed rate, was 383 K. Dried particles were collected using a cyclone at the base of the spray drying chamber and calcined in static air at 823 K for 5 h using a ramp rate of 3 K min^{-1}.

Characterization Methods. Si and Al concentrations in the solids and in the filtrates obtained after the treatments were determined by inductively coupled plasma optical emission spectroscopy (ICP-OES) (Perkin-Elmer Optima 3200RL (radial)). Powder X-ray diffraction (XRD) patterns were measured in a Siemens D5000 diffractometer with Bragg−Brentano geometry and Ni-filtered CuKα radiation (λ = 0.1541 nm). Data were recorded in the range 5−50° 2θ with an angular step size of 0.05° and a counting time of 8 s per step. N_2 isotherms at 77 K were measured in a Quantachrome Quadrasorb-SI gas adsorption analyzer. Prior to the measurement, the samples were degassed in vacuum at 573 K for 10 h. The Brunauer−Emmett−Teller (BET) method[41] was applied to calculate the total surface area, which is used for comparative purposes. The *t*-plot[42] method was used to discriminate between micro- and mesoporosity. The pore size distribution (PSD) was obtained by applying the Barret−Joyner−Halenda (BJH) model[43] to the adsorption branch of the isotherm. High-resolution low-pressure Ar isotherms at 87 K were measured in a Quantachrome Autosorb-1 MP gas adsorption analyzer. Prior to the measurement, the samples were in situ degassed in vacuum at 573 K for 12 h. Free-space measurements were recorded separately to avoid helium entrapment phenomena that adversely affect the adsorption analysis. The PSD was calculated using a hybrid nonlocal density functional theory (NLDFT) model that assumes cylindrical pore geometry.[44] Transmission electron microscopy (TEM) was carried out in a JEOL JEM-1011 microscope operated at 100 kV. A few droplets of the solid sample suspended in ethanol were placed on a carbon-coated copper grid followed by evaporation at ambient conditions. Energy dispersive X-ray (EDX) analysis was carried out in a JEOL JEM-2100 transmission electron microscope coupled to an EDX INCA X-sight analyzer operated at 200 kV. Solid-state magic angle spinning nuclear magnetic resonance (MAS NMR) spectra were recorded at a spinning speed of 15 kHz on a Bruker Avance 700 MHz standard-bore spectrometer equipped with a 2.5 mm BB/1H probe and 2.5 mm ZrO_2 rotors. ^{27}Al spectra were recorded using 2048 accumulations at 2.7 μs pulses, an angle of 90°, and a relaxation time of 1 s, with $NH_4SO_4Al \cdot H_2O$ as a reference. NMR spectroscopy of the filtrates was carried out using a Bruker Avance 500 MHz spectrometer. ^{29}Si NMR spectra were measured at 99.36 MHz, and the chemical shifts were referenced to $Si(CH_3)_4$. ^{27}Al NMR spectra were recorded at 130.32 MHz taking $Al(H_2O)_6^{+3}$ as the reference. Prior to analysis, clear filtrates of the various post-synthesis treatments were diluted (70 vol.%) in D_2O (99.9 at.% D, Aldrich) and loaded in 5 mm i.d. Teflon liners. The spectra were accumulated during 12 h at 278 K. Fourier-transform infrared spectroscopy (FTIR) was performed in nitrogen atmosphere at 473 K on a Thermo Nicolet 5700 spectrometer using a SpectraTech Collector II diffuse reflectance accessory and equipped with a high-temperature cell. Prior to the measurement, the sample was dried at 573 K in N_2 flow (100 cm^3 min^{-1}) for 60 min. Spectra were recorded in the range of 650−4000 cm^{-1} with a nominal resolution of 4 cm^{-1} and co-addition of 64 scans. Temperature-programmed desorption of ammonia (NH_3-TPD) was carried out in a Thermo TPDRO 1100 unit equipped with a thermal conductivity detector. The sample (125 mg) was pretreated at 823 K in He (20 cm^3 min^{-1}) for 2 h. Afterward, pure NH_3 (25 cm^3 min^{-1}) was adsorbed at 473 K for 10 min followed by He purging at the same temperature for 1 h. This procedure was repeated three times. Desorption of

(41) Brunauer, S.; Emmett, P. H.; Teller, E. *J. Am. Chem. Soc.* **1938**, *60*, 309.
(42) Lippens, B. C.; de Boer, J. H. *J. Catal.* **1965**, *4*, 319.
(43) Barrett, E. P.; Joyner, L. G.; Halenda, P. P. *J. Am. Chem. Soc.* **1951**, *73*, 373.
(44) Thommes., M. In *Nanoporous Materials: Science and Engineering*; Lu, G. Q., Zhao, X. S., Eds.; Imperial College Press: London, 2004; pp 317−364.

NH_3 in He flow (20 cm^3 min^{-1}) was monitored in the range of 473−1173 K using a ramp rate of 10 K min^{-1}. Pd dispersion was determined by CO chemisorption using a Quantachrome Autosorb-1C gas sorption system. Prior to CO chemisorption, the sample was pretreated in He at 573 K (5 K min^{-1}) for 30 min, reduced in H_2 (50 cm^3 min^{-1}) at 473 K for 2 h, evacuated at 473 K for 2 h, and cooled down to 308 K in vacuum. Afterward the CO isotherms were recorded. The monolayer volume of adsorbed CO was determined by the dual-isotherm method,[45] in which the adsorption isotherm is recorded two times. The first isotherm quantifies the strong and weak interactions. The second isotherm recorded after evacuation at 308 K represents only weakly adsorbed CO. The difference between the two isotherms comprises the amount of strongly adsorbed CO. An adsorption stoichiometry of CO:Pd = 1:1 was considered in the calculation of the exposed metal area and metal dispersion.

Butane Elution. Elution experiments of butane isomers were carried out at ambient pressure in a quartz microreactor (4 mm i.d.) coupled to an Omnistar GSD 320 O1 (Pfeiffer Vacuum) quadrupole mass spectrometer (MS) for online gas analysis. The zeolite (50 mg, sieve fraction 150−300 μm) was loaded between two layers of quartz wool and rested over a porous frit. The sample was pretreated in argon (100 cm^3 min^{-1}) at 623 K for 30 min and cooled down in the same gas to 363 K. Then, a mixture of 100 Pa *n*-butane (or *i*-butane) in Ar (100 cm^3 min^{-1}) was introduced. The monitored atomic mass unit was 43 for both alkanes. After about 30 min the MS signal was stable. Then, the flow was switched back to pure argon (100 cm^3 min^{-1}) and the elution of the hydrocarbon from the zeolite was followed.

Polyethylene Pyrolysis. Low-density polyethylene (LDPE, powder, Alfa Aesar) pyrolysis was carried out in a Mettler Toledo TGA/SDTA851e microbalance. The polymer (3.75 mg) and the zeolite (1.25 mg), both in powder form, were carefully weighed and intimately mixed in the α-Al_2O_3 crucibles of the thermobalance. The pyrolysis was performed in N_2 (70 cm^3 min^{-1}) ramping the temperature from 303 to 1173 at 10 K min^{-1}.

3. Results and discussion

3.1. Post-Synthesis Modifications. Three successive treatments, involving aqueous solutions of $NaAlO_2$, HCl, and NaOH, were performed to enhance the porosity of the parent ferrierite zeolite (Figure 1). The influence of the sequential post-treatments on the composition, structure, morphology, porosity, and acidity is presented in the next subsections.

Parent Ferrierite. The parent sample (P) comprised a bulk Si/Al ratio of 28 (ICP-OES analysis). Both nitrogen and high-resolution low-pressure argon adsorption isotherms confirmed the microporous nature of the sample (Figure 2). The nitrogen isotherm of the sample is type I, typical of microporous materials in the absence of significant mesoporosity. Concomitantly, the characteristic s-shaped Ar adsorption isotherm evidenced a predominant uptake at $p/p_0 < 0.1$. The obtained characteristic micropore volume (V_{micro} = 0.14 cm^3 g^{-1}) was combined with a relatively low mesopore surface area (S_{meso} = 20 m^2 g^{-1}). Application of the hybrid NLDFT and BJH models yielded the PSDs which show no

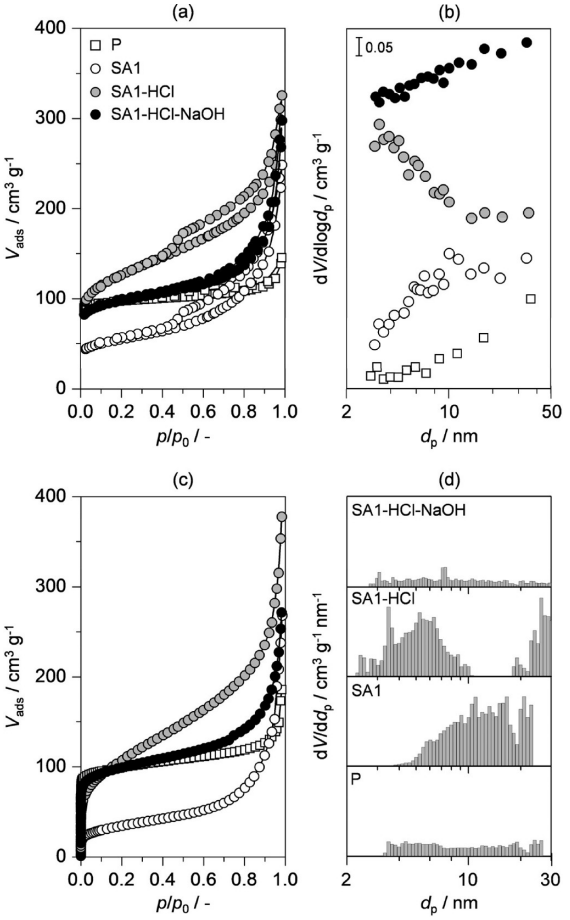

Figure 2. N_2 (a) and Ar (c) isotherms of ferrierite samples. BJH (b) and NLDFT (d) PSDs derived from N_2 and Ar isotherms, respectively. The legend in (a) applies to (b) and (c) as well.

significant contribution in the mesopore region. TEM revealed the typical platelet-like morphology of the ferrierite particles (Figure 3).The X-ray diffractogram exhibited typical reflections of the FER framework as the only crystalline phase (Figure 4). The chemical composition obtained by EDX and ICP-OES analyses was in good agreement. The ^{27}Al MAS NMR spectrum of P showed the typical contributions around 55 ppm (Figure 5), assigned to tetrahedrally coordinated aluminum in the FER lattice.[46]

$NaAlO_2$ Treatment. The ability of aqueous sodium aluminate to leach silicon in ferrierite was screened by contacting the parent sample with 1 M $NaAlO_2$ at different times and temperatures (code SA*x*, Table 1). The porosity of the obtained solids was examined by N_2 adsorption of which the textural properties are summarized in Table 2. Porosity-wise several trends can be rationalized similar to those found previously on ZSM-5.[29] Upon $NaAlO_2$ treatment the mesopore surface area increased (up to 132 m^2 g^{-1} in SA1) as well as the pore volume (up to 0.35 cm^3 g^{-1} in SA1). On the other hand, the treatment causes a strong decrease of the micropore volume and BET surface area (0.01 cm^3 g^{-1} and 147 m^2 g^{-1}, respectively, in SA2). These effects

(45) Groen, J. C.; Pérez-Ramírez, J.; Peffer, L. A. A. *Stud. Surf. Sci. Catal*. **2001**, *135*, 2862–2869.

(46) Sarv, P.; Wichterlová, B.; Čejka, J. *J. Phys. Chem. B* **1998**, *102*, 1372.

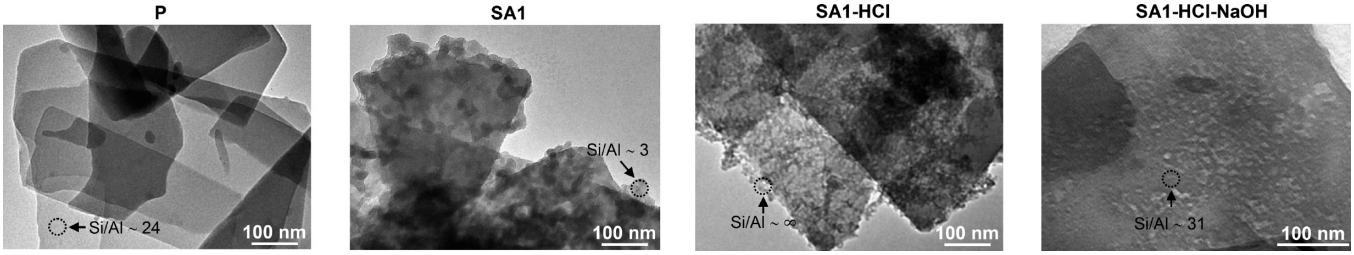

Figure 3. TEM images of ferrierite samples. The displayed Si/Al ratios were determined by EDX analysis.

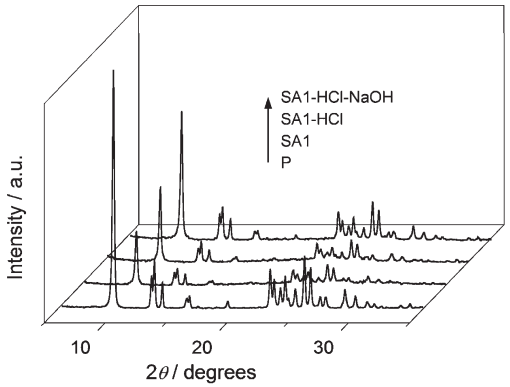

Figure 4. Powder XRD patterns of ferrierite samples.

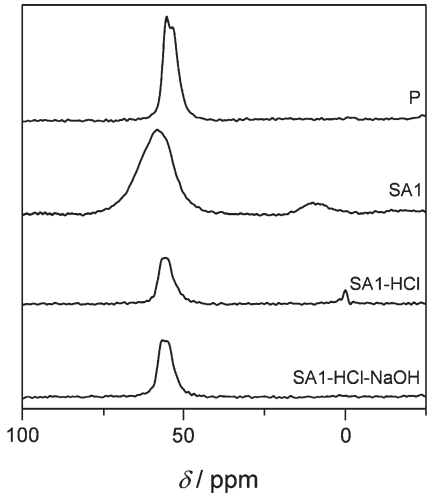

Figure 5. Solid-state ^{27}Al MAS NMR of ferrierite samples.

initially increased with time and temperature, but remained fairly constant when reaction time was longer than 3 h (6 h, in SA2) or reaction temperature was higher than 353 K (363 K, in SA3). We focus on describing the physicochemical properties of the SA1 sample, in which a high degree of mesoporosity was introduced. Characterization results of samples at other $NaAlO_2$ treatment conditions are qualitatively equivalent and are not shown for conciseness. The N_2 isotherm of SA1 evidence that the uptake at lower relative pressures was reduced greatly whereas the uptake at middle-to-high relative pressures increased (Figure 2a). The BJH PSD of SA1 indicates the presence of mesopores centered roughly around 10 nm (Figure 2b). These observations are nicely confirmed by the Ar isotherm and related mesopore size distribution

Table 2. Porous Properties of Parent and Treated Ferrierite Zeolites and Yield of the Treatments

sample	V_{pore} [a] ($cm^3\ g^{-1}$)	V_{micro} [b] ($cm^3\ g^{-1}$)	S_{meso} [b] ($m^2\ g^{-1}$)	S_{BET} [c] ($m^2\ g^{-1}$)	yield [d] (%)
P	0.22	0.14	20	369	-
SA1	0.35	0.03	132	199	136
SA2	0.32	0.01	126	147	144
SA3	0.33	0.01	132	162	134
SA4	0.25	0.08	63	265	108
SA5	0.24	0.11	47	316	107
HCl	0.22	0.14	23	356	99
SA1-HCl	0.46	0.12	185	461	56 (76)
SA2-HCl	0.44	0.10	179	411	57 (82)
SA3-HCl	0.37	0.10	131	360	65 (87)
SA4-HCl	0.28	0.12	53	351	81 (88)
SA5-HCl	0.24	0.13	55	358	83 (89)
NaOH	0.22	0.14	26	357	93
SA1-HCl-NaOH	0.41	0.11	99	363	54 (41)
SA1-NaOH	0.35	0.03	84	164	85 (129)
SA1-NaOH-HCl	0.49	0.09	199	410	74 (96)

[a] N_2 adsorption, volume adsorbed at $p/p_0 = 0.99$. [b] t-plot. [c] BET method. [d] Individual step yield, in grams of solid after treatment per gram of starting material (overall yield with respect to parent zeolite in brackets).

Table 3. Chemical Composition of the Solids and Filtrates upon Different Treatments of Ferrierite

sample	Si/Al_{solid} (-)	$[Si]_{filtrate}$ (ppm)	$[Al]_{filtrate}$ (ppm)
P	28	-	-
SA1	3	292	10587
SA1-HCl	42	44	2017
SA1-HCl-NaOH	22	4055	10
SA1-NaOH	3	444	91
SA1-NaOH-HCl	39	58	7078

(Figures 2c and 2d, respectively). At this initial stage of the treatment sequence, the origin of the introduced mesoporosity cannot be ascertained. The pronounced increase in weight (up to 44% in SA2) of the samples after treatment (Table 2) indicates that species where deposited during the reaction. Additionally, the bulk Si/Al ratio decreased significantly from 28 (in P) to 3 (Table 3). The loss of microporosity, the decrease in Si/Al ratio, and high yield can accurately be explained by the considerable deposition of $Al(OH)_3$ (Al_2O_3 upon calcination) on the zeolite, which block the accessibility of Ar and N_2 to the micropores. TEM and EDX analyses confirm the presence of amorphous Al-rich species situated on the surface of the ferrierite platelets (Figure 3). The diffraction pattern of SA1 (Figure 4) shows a strong loss of intensity of the characteristic reflections of the FER framework and the absence of any other crystalline phases. These observations are attributed to the presence

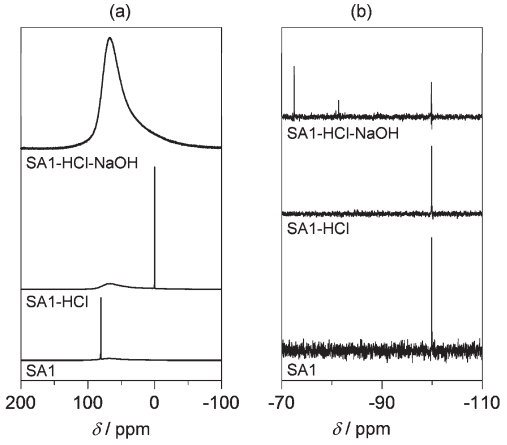

Figure 6. ^{27}Al (a) and ^{29}Si (b) NMR spectra of the filtrates resulting from each post-synthesis treatment applied to ferrierite.

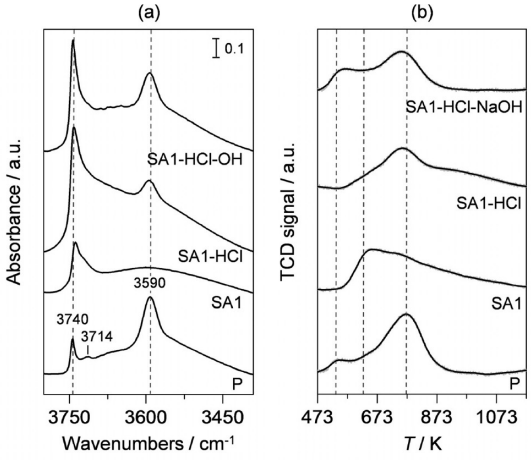

Figure 7. Infrared spectra in the OH stretching region (a) and NH_3-TPD profiles (b) of ferrierite samples.

of amorphous debris and the introduction of intracrystalline mesoporosity in the ferrierite crystals. The latter typically reduces the intensity of the diffraction lines because of shortening of the intracrystalline domains upon mesopore formation and certain local amorphization.[18] Solid-state ^{27}Al MAS NMR revealed that the typical contributions due to tetrahedral Al in the FER framework at about 55 ppm are not distinguishable in SA-1 (Figure 5). This is due to the appearance of broad peaks at 59 ppm and 10 ppm. These peaks are characteristic of alumina,[47,48] which is deposited on the zeolite crystals.

ICP-OES (Table 3) and liquid-state NMR (Figure 6) analyses of the filtrates were carried out to gain further insights into the chemical species extracted from the zeolite. As expected the filtrate contained a large amount of Al. On the other hand, the filtrate comprised relatively few Si entities (ca. 300 ppm) compared to that typically obtained after NaOH-mediated desilication (roughly 5000 ppm).[18] The ^{27}Al NMR spectrum of the SA1 filtrate shows signals at 69.7 and 80.8 ppm. The sharp and more predominant peak at 80.8 ppm corresponds to the aluminate anion AlO_4^{-5}.[49] The peak at 69.7 ppm corresponds to $Al(OSi)_2$ sites,[50] which are related to aluminosilicate species. The broadness of this signal is the result of the anisotropic electric surrounding of the aluminum.[51] Whether these aluminosilicates come directly from the zeolite or are the product of AlO_4^{-5} combining with small amounts of leached silicon cannot be ascertained. The ^{29}Si NMR spectrum of the SA1 filtrate exhibits a single peak near −100 ppm, assigned to cubic octamers,[52] which suggests that the few Si entities that were extracted during $NaAlO_2$ treatment did not fully dissolve.

Dramatic changes in the acid properties of the SA*x* samples were observed by infrared spectroscopy in the OH stretching region and by NH_3-TPD (Figure 7). The typical Brønsted acid site band at 3590 cm^{-1} present in the parent zeolite, P, disappeared after the treatment, which is attributed to the sodium/proton ion exchange occurring during $NaAlO_2$ treatment. Efforts regarding an additional ion exchange to restore the proton were not included as this treatment could influence the aluminum-containing deposits characteristic to this sample. Additionally, the small peak in P at 3714 cm^{-1}, ascribed to weakly perturbed Si−OH inside the zeolite crystal,[23] was masked by the broad band associated with Al−OH stretching vibrations of the Al_2O_3-deposits. The isolated surface silanol band at 3740 cm^{-1} did not grow as is typically the case after controlled mesopore development in the zeolite crystal by NaOH-based alkaline leaching.[18,22] Likely, Al debris precipitated on top of the zeolite crystals covering a significant fraction of the silanol groups. In line with the results obtained by infrared spectroscopy, the NH_3-TPD profile of SA1 shows that the intrinsic Brønsted peak at 770 K in the parent ferrierite practically vanished. Additionally, a new peak is observed at 650 K. This peak can be ascribed to acid sites of Lewis nature related to aluminum debris deposited during the SA treatment.[29]

HCl Treatment. To eliminate Al deposits from the modified zeolites and to restore the protonic form, an acid wash using HCl was carried out. Table 2 shows the influence of the acid wash on the porosity of various samples (Code HCl or SA*x*-HCl). The influence of this treatment on the parent ferrierite proved sterile as expected from the remarkable stability of this framework in acid medium.[36−40] However, in case of the sodium aluminate-treated samples microporosity had almost completely restored upon hydrochloric acid washing. The V_{micro} increased from 0.03 cm^3 g^{-1} (SA1) to 0.12 cm^3 g^{-1} (SA1-HCl). The mesopore surface area remained mostly the same for the SA*x*-HCl samples; however, at 353 K (SA1-HCl and SA2-HCl) the mesoporosity increased too. Accordingly, the corresponding N_2 and

(47) Brew, D. R. M.; MacKenzie, K. J. D. *J. Mater. Sci.* **2007**, *42*, 3990.
(48) Zhang, W.; Sun, M.; Prins, R. *J. Phys. Chem. B* **2003**, *107*, 10977.
(49) Goudarzi, N.; Goodarzi, M.; Arab-Chamgangali, M.; Bagherian, G. *J. Mol. Struct.* **2009**, *930*, 2.
(50) Müller, D.; Gessner, W.; Samoson, A.; Lippmaa, E.; Scheler, G. *J. Chem. Soc., Dalton Trans.* **1986**, 1277.
(51) Harris, R. K.; Samadi-Maybodi, A.; Smith, W. *Zeolites* **1997**, *19*, 147.
(52) Fan, W.; Meneau, F.; Bras, W.; Ogura, M.; Sankar, G.; Okubo, T. *Microporous Mesoporous Mater.* **2007**, *101*, 134.

Ar isotherms of SA1-HCl showed increased uptake at low relative pressures and maintained their uptake at middle-to-high relative pressures (Figure 2). The BJH PSD (Figure 2b) reveals that the mesopores in SA1-HCl are centered around 5 nm, which contrasts with the non-centered PSDs obtained in FER by conventional desilication using NaOH.[18] Hybrid NLDFT modeling further confirmed that the PSD was centered around 5 nm (Figure 2d). The low yields (down to 56% for SA1-HCl, with respect to SA1) indicate a large weight loss upon HCl washing (Table 2). Table 3 shows that the Si/Al ratio has increased from 3 in SA1 to 42 in SA1-HCl, which implies that all deposited Al was successfully removed. In fact, the Si/Al ratio exceeds the ratio in P (28), and therefore some Al originating from the parent sample must have been additionally removed. Most likely this Al comprises Lewis acid sites which, unlike the Brønsted acid sites, are more easily leached by acid washing.[26] TEM analysis shows that the amount and morphology of deposits in SA1-HCl drastically changed compared to SA1. The surface debris on SA1-HCl appear smaller and rougher compared to those on SA1 (Figure 3). Surprisingly, EDX analysis shows that the remaining debris on SA1-HCl comprise mostly silicon. We suspect that during the sodium aluminate treatment Si debris are leached from the zeolite framework and covered with the Al debris. Subsequently, when the aluminum deposits are removed the Si debris are exposed. Likely, the latter debris contribute significantly to the porous nature of SA1-HCl, for example, they could be to a certain extent responsible for the increase in S_{meso} of SA1-HCl and SA2-HCl compared with SA1 and SA2, respectively. The acid wash resulted in increased crystallinity (Figure 4), which is attributed to the removal of the amorphous Al-containing debris and the concomitant increase of zeolite fraction in the sample. Solid-state ^{27}Al MAS NMR corroborates the removal of the Al-rich debris as peaks at 59 ppm and 10 ppm disappeared completely whereas the typical FER framework Al peak at about 55 ppm returned (Figure 5). Additionally a small peak at 0 ppm appeared which can be attributed to octahedral (extra-framework) Al present in the Si-rich debris (vide infra).[18,53]

ICP-OES analysis on the filtrate (Table 3) shows that mostly Al is removed (and additionally some Si). The ^{27}Al NMR spectrum of the filtrate reveals that in the acidic solution Al is present as its solvated octahedrally coordinated cation $Al(OH_2)_6^{3+}$ at 0 ppm (Figure 6a). The small peak at 69.7 ppm, associated with aluminosilicates, has increased slightly compared to the spectrum of the SA1 filtrate, which should be related to the relative increase of Al-containing zeolite framework fragments in the filtrate. The peak at -100 ppm in the ^{29}Si NMR spectrum shows that the only released Si entities were those related to cubic octamers. We put forward that a small fraction of Si entities, most likely completely entrapped by Al debris, was released from the sample upon acid washing.

Assessment of the acid properties of SA1-HCl reveals that the signal at 3590 cm^{-1} associated with Brønsted acid sites reappeared. This follows from the ion exchange that has taken place during HCl treatment restoring the protonic form of the zeolite. In the infrared spectrum the silanol band (3740 cm^{-1}) appears more intense with respect to the SA1 sample, which could be attributed to the removal of aluminum-containing debris blocking the isolated surface silanols. The NH_3-TPD profile of SA1-HCl corroborates the recovery of the Brønsted acidity feature at 770 K. Naturally, as large amounts of aluminum-containing deposits were removed, the peak at 650 K belonging to strong Lewis acid sites was strongly decreased.

NaOH Treatment. In view of its complex nature an alkaline washing was performed to remove the Si-rich debris from sample SA1-HCl. It is commonly known that high-silica zeolites and silicas are easily dissolved by mild alkaline treatment using aqueous NaOH.[54,55] The influence of such a mild base leaching treatment (0.2 M NaOH, 338 K, 30 min) on the parent ferrierite was negligible (Table 2). This was as expected as the Al-containing FER framework requires harder conditions to be desilicated (e.g. 0.5 M NaOH, 353 K, 3 h).[18] This enables this treatment to be used to selectively remove the Si debris formed in the $NaAlO_2$ step from the ferrierite crystals. An extra alkaline washing was not previously considered in connection with the two-step $NaAlO_2$ and HCl treatment.[29,30] Table 2 shows that the alkaline wash had a severe influence as the yield relative to sample SA1-HCl was only 54%. The porous properties of SA1-HCl-NaOH evidence that the mesopore surface area has nearly halved (to 99 m^2 g^{-1}), and the microporosity was preserved. Accordingly, the N_2 and Ar isotherms show that the uptake at low relative pressures was largely unaffected, whereas the uptake at higher relative pressure was significantly reduced (Figure 2). The PSDs revealed that no centered mesoporosity remained after alkaline washing. TEM images showed the absence of debris on the ferrierite platelets. Instead small holes are present likely to cause intracrystalline mesoporosity (Figure 3). ICP-OES analysis evidenced that the bulk Si/Al ratio in SA1-HCl-NaOH decreased to 22 (Table 3), which implies that the removed material comprised mostly silicon. Clearly, upon alkaline washing the debris are removed along with half of the mesopore surface area and the centered PSD. In fact, the obtained mesopore surface area, the BJH PSD, and overall yield (41%) show striking resemblance to the hierarchical ferrierite obtained by one-step desilication with NaOH.[18] We conclude that the mechanism of mesopore formation in ferrierite using aqueous sodium aluminate is similar compared to the one involving aqueous NaOH. However the distinct nature of the $NaAlO_2$ solution leads to significant Al precipitation in the leaching process, which covers most of the surface of the zeolite and

(53) Deng, F.; Du, Y.; Ye, C.; Wang, J.; Ding, T.; Li, H. *J. Phys. Chem.* **1995**, *99*, 15208.

(54) Čižmek, A.; Subotić, B.; Aiello, R.; Crea, F.; Nastro, A.; Tuoto, C. *Microporous Mater.* **1995**, *4*, 159.

(55) Niibori, Y.; Kunita, M.; Tochyama, O.; Chida, T. *J. Nucl. Sci. Technol.* **2000**, *37*, 349.

Table 4. Phase Composition and Crystallinity of the Solids upon Different Treatments of Ferrierite

	phase[a]			peak intensity[b]	
sample	Zeolite (-)	Si debris (-)	Al debris (-)	measured (%)	calculated[c] (%)
P	100			100	100
SA1	41	35	60	21	16
SA1-HCl	41	35		30	29
SA1-HCl-NaOH	41			54	54

[a] Based on the overall yields (Table 2, last column in brackets), relative to P. [b] (200) reflection at about 9° 2θ (Figure 4), relative to P. [c] According to the zeolite phase fraction, corrected for intensity loss because of the introduction of intracrystalline mesoporosity (100−54 = 46%, based on SA1-HCl-NaOH).

blocks the evacuation and dissolution process of Si entities extracted from the ferrierite zeolite framework. Accordingly, the relatively high Si/Al ratio of the mesoporous zeolites obtained by the two-step $NaAlO_2$ sequence[29] versus NaOH treatment[18] (26 vs 19 when starting from Si/Al ratio 27) is attributed to the remaining Si debris in the sample. This implies that samples obtained by combined two-step $NaAlO_2$+HCl treatment in previous studies[29,30] comprised also such composites of intracrystalline ferrierite and Si-rich deposits. Clearly, the Si-rich debris situated in and on the ferrierite platelets contribute significantly to the mesoporosity and related centered PSD. Consequently, the mesopore surface area of the SA*x*-HCl samples comprises a combination of intracrystalline mesopores related to the leaching of Si from the ferrierite crystals and intercrystalline mesoporosity because of the silicon debris. The centered PSDs derived from N_2 and Ar adsorption related to SA1-HCl suggest that the particles are uniform in size. Considering the significant presence of silicon debris in SA1-HCl (46 wt %) and the similar V_{micro} in SA1-HCl and SA1-HCl-NaOH, the Si debris should exhibit significant microporosity as well. The presence of microporosity implies that the Si debris must have crystalline nature. Nevertheless, they are not detectable by XRD, which suggests, in line with TEM observations, that they must be small nanocrystals. On the basis of the overall yields of the $NaAlO_2$ treatment and both acid and alkaline washing steps, we estimated the composition of the samples, that is, the relative abundance of zeolite, Al debris, and Si debris. Table 4 shows that SA1 is a composite of which only 30 wt % is related to intrinsic zeolite material, and the remaining 70 wt % comprise Al debris (44 wt %) and Si debris/nanocrystals (26 wt %). The Al debris are removed after the acid wash and a composite of zeolite (54 wt %) and Si debris (46 wt %) is obtained. The subsequent NaOH wash leads to a debris-free hierarchical ferrierite. The loss of intensity of the XRD pattern due to the introduction of intracrystalline mesoporosity (46%) can be determined by comparing the parent zeolite (100% relative intensity) to the debris-free hierarchical ferrierite (SA1-HCl-NaOH, 54% relative intensity). This correction is in line with what was reported for mesoporous ferrierite prepared by NaOH treatment.[18] By additionally taking into account the reduction of intensity because of the presence of debris in the samples, it proved that the intensities of samples SA1 and SA1-HCl agree quite well with the calculated values (Table 4). The ^{27}Al MAS NMR spectrum of SA1-HCl-NaOH (Figure 5) shows that with the removal of the Si-rich debris the peak at about 55 ppm remained whereas the peak 0 ppm disappeared. We tentatively conclude that these octahedral Al entities comprised extra-framework aluminum species present in the Si-rich nanocrystals.

The ICP measurements of the filtrate of SA1-HCl-NaOH show that few Al (10 ppm) and large amounts of Si species were present (ca. 4000 ppm, Table 3). The ^{27}Al NMR spectrum of the filtrate evidence the sole presence of the peak assigned to aluminosilicates (69.7 ppm). The ^{29}Si NMR spectrum evidence that more types of Si species were present in the spectrum in addition to the peak attributed to cubic octamers (−100 ppm). The most intense peak appears at −72.5 ppm is associated to monomeric species of silicon. Additional less-intense peaks of dimeric species were obtained at −80.8 ppm and −81.3 ppm. Finally, a trimeric species was identified at −82.6 ppm.[51] The presence of these different forms of silicon in solution relates to the Si dissolution induced by the alkaline wash. This dissolution was not evidenced in the SA1 filtrate because of the formation of the Al deposits which inhibited evacuation and covered the Si-rich nanocrystals. Likely, in accordance with solid-state MAS NMR, some of the removed Si nanocrystals contain aluminum, attending to the aluminosilicate peak at −69.7 ppm in the ^{27}Al NMR spectra.

The SA1-HCl-NaOH sample was ion-exchanged with aqueous NH_4NO_3 and calcined to study its acidic properties. The infrared spectrum of the NaOH-washed sample evidenced a more defined band at 3590 cm^{-1} associated with the Brønsted acid sites (Figure 7a). This increase results from the larger fraction of zeolitic material in the sample, as quantified in Table 4. The decrease of the surface silanol groups (3740 cm^{-1}) is likely due to the removal of the small high-surface area Si-rich nanocrystals. Although no band assigned to extra-framework aluminum (3645 cm^{-1}) was present,[22] the NH_3-TPD profile of SA1-HCl-NaOH showed that some Lewis acidity is present, as revealed by the desorption at 540 K (Figure 7b). This peak was also observed in the parent zeolite, but it was not detected after treatment with $NaAlO_2$ and HCl. This could be due to the presence of weak Lewis acid sites, which, in samples SA1 and SA1-HCl, were likely covered by Si and/or Al-containing debris.

It should be pointed out that additional characterization of the series of ferrierite samples (P, SA1, SA1-HCl, SA1-HCl-NaOH) by FTIR spectroscopy of probe

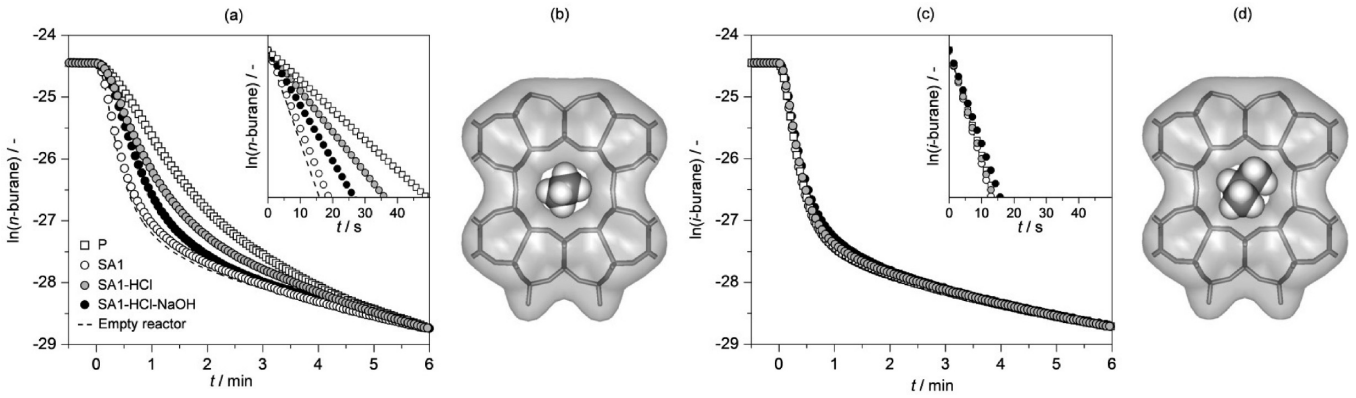

Figure 8. Concentration profiles of *n*-butane (a) and *i*-butane (c) in elution experiments over ferrierite samples. The insets in (a) and (c) show the linear part of the elution profiles. The accessibility of *n*-butane (b) and *i*-butane (d) to the ferrierite 10-ring micropore is illustrated. The profile of the empty reactor (dashed line) is included as a reference.

molecules (substituted alkylpyridines and CO) would have been highly suitable to quantitatively determine the nature of the acid sites and their accessibility, as well as the acid strength.[20,21,23,26] However, we must stress that both IR in the ν_{OH} region and NH_3-TPD are well established methods in zeolite characterization, and their combination provided a solid picture of the pronounced acidity changes upon different post-treatments of ferrierite. Besides, we conducted catalytic tests in LDPE pyrolysis (vide infra), which nicely complemented the acidity characterization.

Influence of the Washing Sequence. Additional experiments were performed on SA1 to clarify the effect of the order of the washing steps. When the $NaAlO_2$-treated zeolite was first washed with aqueous NaOH (to yield SA1-NaOH), the microporosity remained 0.03 $cm^3\ g^{-1}$, and the mesopore surface area reduced down to 84 $m^2\ g^{-1}$ (Table 2). The high yield relative to SA1 (85%) indicates that the SA1-NaOH alkaline washing step was far less efficient in removing Si debris compared to one performed to yield sample SA1-HCl-NaOH (54% yield). ICP-OES analysis evidenced only a tenth of the Si in the filtrate (ca. 400 ppm) compared to the SA1-HCl-NaOH filtrate. This is attributed to the surface coverage of the Al debris that inhibited the Si dissolution process by entrapping the Si-rich nanocrystals. Nevertheless the partial removal of Si suggests that not the entire surface of SA1 is covered with Al debris. Therefore the intercrystalline mesoporosity of the SA*x* samples should be ascribed to both the Si nanocrystals and the Al debris. The filtrate related to sample SA1-NaOH contained a relatively large amount of leached Al (ca. 90 ppm), which is attributed to the removal of Al entities that were entrapped by Si deposits and removed during the NaOH treatment. Nevertheless, as the majority of Al debris remained in the sample, the bulk Si/Al ratio before and after the NaOH wash was similar (3). When subsequently the HCl wash was performed, microporosity was largely restored and an impressive 199 $m^2\ g^{-1}$ of mesopore surface area was obtained. These developments are attributed to the clearing of Al debris from the micropores and the uncovering of residual mesoporous Si-rich nanocrystals. The high relatively high overall yield (96% vs 41% of SA1-HCl-NaOH) and the high Si/Al ratio of SA1-NaOH-HCl (39) confirmed that a large fraction of Si-nanocrystals remained on the sample. Evidently, to remove all silicon nanocrystals the HCl step should be executed first (Figure 1). Clearly, the sequence of modifications is a critical parameter in the design of hierarchical architectures.

3.2. Functions of the Hierarchical Zeolites. *Elution of Butanes*. To study transport we have performed elution experiments over the P, SA1, SA1-HCl, and SA1-HCl-NaOH using alkanes of different kinetic diameters, that is, *n*-butane (0.43 nm) and *i*-butane (0.50 nm). The use of these molecules in elution is particularly insightful as their kinetic diameters are rather similar to the pore size of the ferrierite 10-ring micropores (0.42 × 0.54 nm). A constant diluted feed was applied to obtain steady-state occupancy inside the reactor and zeolites. After switching to pure argon the concentration of *n*-butane and *i*-butane was monitored as a function of time to evaluate their molecular mobility in the samples. Figure 8a shows that the elution of *n*-butane was slowest for P followed by SA1-HCl, SA1-HCl-NaOH, SA1, and the empty reactor (reference), respectively. The order of the ferrierite samples, emphasized by the inset in Figure 8a, relates moderately well with their micropore volumes (Table 2). The strong dependency of the elution rate to the microporous nature of the zeolites demonstrates the diffusion constraints that *n*-butane undergoes in the ferrierite micropores. The tight fit of *n*-butane in the 10-ring micropore channels of ferrierite is visualized in Figure 8b. Although SA1-HCl and SA1-HCl-NaOH have a similar micropore volume, the elution took place remarkably slower over the former sample. We put forward that the microporosity or heterogeneity of the Si-rich nanocrystals, in combination with partial blocking of intrinsic ferrierite micropores, slowed down the elution.

Elution curves measured with *i*-butane show that the elution rates are significantly higher compared to ones obtained using *n*-butane (Figure 8c). In fact, the elution rates of the zeolites and the empty reactor are practically the same. This apparent insensitivity to the porosity of the samples is attributed to the higher kinetic diameter of

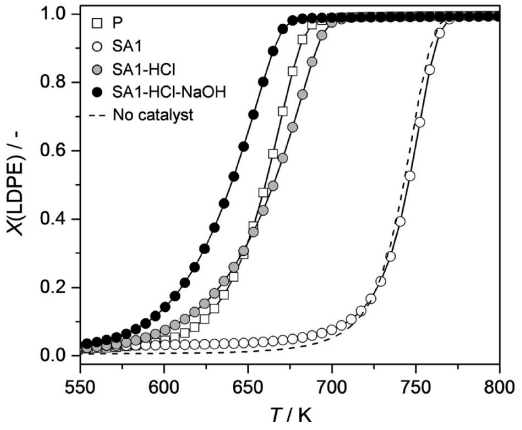

Figure 9. Conversion of low-density polyethylene versus temperature over ferrierite samples. The profile without catalyst (dashed line) is included as a reference.

i-butane (Figure 8d). Unlike in the case of *n*-butane, the branched butane isomer could not enter the micropores and the subsequent elution was not slowed down. Additionally, this proved that C4 alkanes do not suffer from significant diffusion constraints in the mesopores.

Our observations concerning the elution of butane isomers from the ferrierite samples support pore mouth catalysis as evidenced to take place in a number of alkanes/alkenes isomerization reactions on small pore zeolites.[33,56−58] As the branched isomer is not able to be formed inside the pores, the isomerization reaction takes place at the Brønsted sites located at the end of the micropore channels or pore mouths. By introducing intracrystalline mesopores the number of pore mouths, that is, active sites, can be increased dramatically.[20] Consequently, we anticipate an advantageous application of hierarchical porous 10-ring zeolite catalysts in alkane/alkene isomerization processes.

Pyrolysis of Polyethylene. The distinct ferrierites obtained in each post-synthesis treatment were evaluated in the acid-catalyzed degradation of low-density polyethylene. This bulky branched polymer suffers from limited access to the acid sites in the zeolite pore systems,[59] and its pyrolysis is a suitable test reaction to evaluate the beneficial catalytic effects of the introduced mesoporosity versus compromised microporosity.[18,20,60] The catalytic performance was followed by thermogravimetric analysis. A mixture of solid catalyst mixed intimately with LDPE powder was heated to obtain weight loss profiles as a function of temperature (Figure 9). The uncatalyzed pyrolysis shows that 50% of LDPE is converted into gaseous products at 750 K, that is, T_{50} = 750 K. The introduction of the parent ferrierite lowered T_{50} by about 85 K. SA1 did not display any catalytic activity.

Table 5. Palladium Dispersion in the Pd/Ferrierite Samples

sample	Pd[a] (wt %)	Pd surface area[b] ($m^2\ g^{-1}$)	Pd dispersion (%)
P	1.2	0.9	16
SA1-HCl-NaOH	1.4	1.5	26

[a] ICP-OES. [b] Volumetric CO chemisorption.

On the other hand, SA1-HCl-NaOH (T_{50} = 635 K) displayed improved performance compared to P by about 30 K, which proves that intracrystalline mesopores enhance LDPE pyrolysis. SA1-HCl shows a similar profile to the parent zeolite, indicating that the Si-rich nanocrystals do not enhance conversion in pyrolysis. This catalytic inactivity should be related to the lack of framework Al in the nanocrystals, that is, the lack of Brønsted acidity. Additionally, the intercrystalline mesoporosity does not increase the accessibility or number of the pore mouths. The lower pyrolysis performance of SA1-HCl compared to SA1-HCl-NaOH should be therefore attributed to the intrinsic inactivity of the Si-rich nanocrystals and possibly to the reduced access of the LDPE polymer to the intracrystalline mesopores because of blocking caused by such nanocrystals.

Palladium Dispersion. Zeolites are frequently used as a host for metallic species, for example, as bifunctional catalysts, in which they serve a dual purpose. First, their acidity is utilized in catalysis, and second, they act as support material to lower noble metal particle sizes. A lower particle size is of significance as hereby the number of active sites per gram of noble metal is increased, which in turn, in many cases, leads to enhanced catalytic performance.[61] The functionality of mesoporous zeolites to increase dispersion was established by Christensen et al.[62] They visualized (by TEM) improved dispersions of Pd in thermally activated catalysts prepared by wet impregnation of a Pd precursor on hierarchical ZSM-5 prepared by carbon templating. However, a thorough quantification of the influence of the mesoporosity on the noble metal particle size distribution was not provided. Here we have evaluated the functionality of both purely microporous (P) and hierarchical ferrierite (SA1-HCl-NaOH) containing Pd particles deposited by means of spray drying. The spray drying methodology is widely employed in the food and pharmaceutical industry or for granulation of inorganic materials. This work shows its usefulness in metal deposition. According to ICP-OES analysis, the Pd deposition in the P and SA1-HCl-NaOH samples rendered 1.2 and 1.4 wt %, respectively (Table 5), which is close to the target loading (1.3 wt % Pd). The effect of the introduction of intracrystalline mesoporosity in thermally activated ferrierite on the size and uniformity of the Pd particles is nicely visualized in Figure 10. The TEM images show that the particles deposited on P are bigger and less consistent in size compared to

(56) Lee, S.-H.; Shin, C.-H.; Hong, S.-B. *J. Catal.* **2004**, *223*, 200.
(57) Houzvicka, J.; Ponec, V. *Catal. Rev. -Sci. Eng.* **1997**, *39*, 319.
(58) Martens, J. A.; Souverijns, W.; Verrelst, W.; Parton, R.; Froment, G. F.; Jacobs, P. A. *Angew. Chem., Int. Ed. Engl.* **1995**, *34*, 2528.
(59) Agullo, J.; Kumar, N.; Berenguer, D.; Kubicka, D.; Marcilla, A.; Gómez, A.; Salmi, T.; Murzin, D. Y. *Kinet. Catal.* **2007**, *48*, 535.
(60) Pérez-Ramírez, J.; Abelló, S.; Bonilla, A.; Groen, J. C. *Adv. Funct. Mater.* **2009**, *19*, 164.
(61) van Santen, R. A.; van Leeuwen, P. W. N. M.; Moulijn, J. A.; Averill, B. A. *Catalysis: An Integrated Approach*, 2nd ed.; Elsevier: Amsterdam, 1999; pp 29−80.
(62) Christensen, C. H.; Schmidt, I.; Carlsson, A.; Johannsen, K.; Herbst, K. *J. Am. Chem. Soc.* **2005**, *127*, 8098.

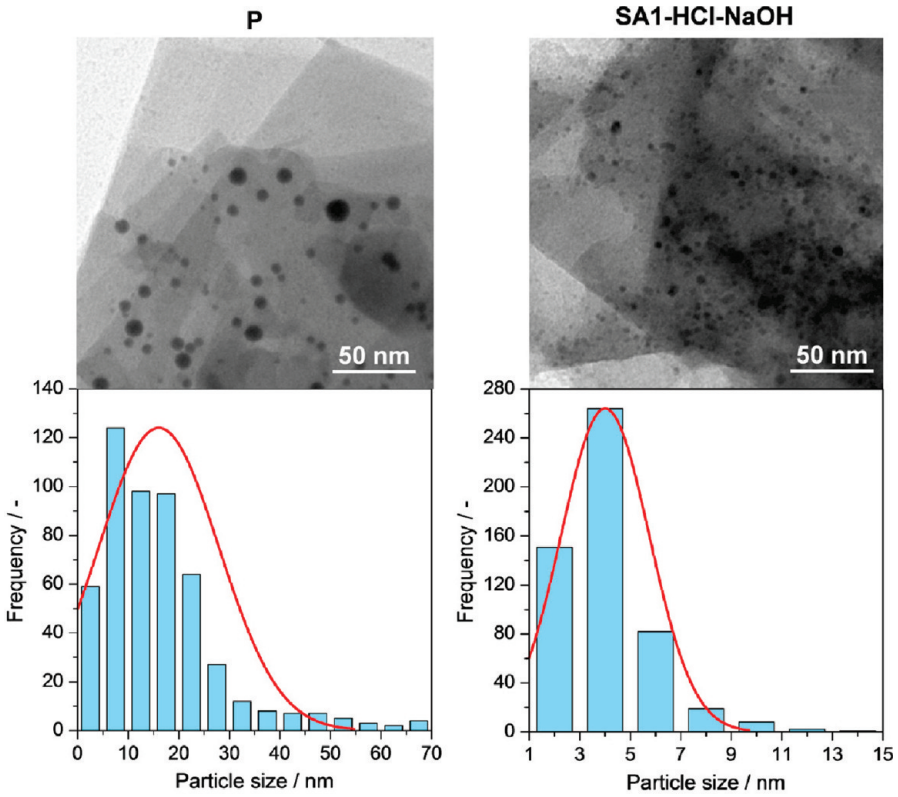

Figure 10. TEM images of Pd/ferrierite samples (top) and corresponding histograms of palladium particle size distribution (bottom).

SA1-HCl-NaOH. This is confirmed by the statistical particle size distributions (bottom of Figure 10), which are based on the visual inspection of TEM pictures in which at least 500 Pd particles per sample were measured. These distributions show that for P the particle sizes are centered around 15 nm and for the mesoporous ferrierite near 4 nm. Additionally the particle size distribution is narrower for the mesoporous sample which confirms that particles deposited on zeolites with intracrystalline mesopores are both smaller and more homogeneous in size. NH_3-TPD and FTIR analyses of the Pd/zeolites (data not shown) evidenced that the acidity properties as presented in Figure 7 were not altered. The deposition of Pd particles on mesoporous ferrite was quantified by CO chemisorption.[45] Remarkably, even though the loading was higher on SA1-HCl-AT, the exposed Pd surface area per gram sample was significantly 67% higher in SA1-HCl-AT (1.5 $m^2\ g^{-1}$) compared to the parent zeolite (0.9 $m^2\ g^{-1}$). Accordingly, the palladium dispersion of P is 16% while for SA1-HCl-NaOH dispersion of 26% was obtained (Table 5). Clearly, the introduction of intracrystalline mesoporosity in ferrierite has a positive influence on the resulting Pd dispersion.

4. Conclusions

A sequence of post-synthesis zeolite modifications was performed that generated different hierarchical porous structures from typically sterile ferrierite. The composition, structure, morphology, porosity, and acidity was influenced distinctly which was attributed to the presence of Si and Al deposits and the formation of intracrystalline mesoporosity. Upon sodium aluminate treatment the formation of intracrystalline mesopores took place concurrently with the substantial deposition of Al debris and Si nanocrystals, which resulted in a combined intra-and intercrystalline mesopore surface area of up to 136 $m^2\ g^{-1}$. The Al debris covered nearly completely the ferrierite crystals and consequently blocked the micropores. After an acid wash the Al debris were removed restoring microporosity and uncovering hierarchical porous Si nanocrystals which increased the mesoporosity (up to 185 $m^2\ g^{-1}$). Subsequently, an alkaline wash was performed that removed the silicon nanocrystals and concomitantly the intercrystalline mesoporosity. This NaOH wash reduced the mesopore surface area to a typical 99 $m^2\ g^{-1}$, attributed to intracrystalline mesopores. The order of the acid and alkaline washing steps proved of crucial importance. The mechanism of introduction of intracrystalline mesoporosity was similar using aqueous $NaAlO_2$ compared to the use of aqueous NaOH. The presence of the silicon and aluminum debris did not enhance transport or performance in LDPE pyrolysis. On the other hand, the debris-free sample with intracrystalline mesoporosity showed enhanced transport and catalytic performance. Finally, we proved that Pd particles deposited by a novel spray drying method are more finely and homogenously dispersed over mesoporous ferrierite.

Acknowledgment. This research was supported by the Spanish MICINN (CTQ2009-09824/PPQ and Consolider-Ingenio 2010, Grant CSD2006-0003) and the ICIQ Foundation.